Advances in Water Resources 218 (2026) 105522

Contents lists available at ScienceDirect

Advances in Water Resources

journal homepage: www.elsevier.com/locate/advwatres

Hydrodynamic shielding and non-monotonic mass transfer in porous media convection

Yumin Wang [a,b], Jiansong Wu [a,*], Ke Xu [b]

[a] School of Emergency Management and Safety Engineering, China University of Mining and Technology - Beijing, Beijing, 100083, China
[b] Department of Energy and Resources Engineering, College of Engineering, Peking University, Beijing, 100871, China

ARTICLE INFO

Keywords:
Buoyancy-driven convection
Porous media
Wavy interface
Non-monotonic mass transfer
Hydrodynamic shielding

ABSTRACT

Dissolution fronts, thawing fronts and geological contacts can form wavy interfaces that regulate solute exchange in porous media. We use two-dimensional Darcy–Brinkman simulations above a fixed sinusoidal boundary to examine how wave count, amplitude and Rayleigh number affect mass transfer and concentration redistribution. Boundary flux and concentration statistics are averaged over matched time windows. The results show that developing convection enhances transfer, with the gain depending on wave count and amplitude. Under vigorous convection, the Sherwood number increases with Rayleigh number while their ratio generally declines, indicating that mass transfer increases less than proportionally with Rayleigh number. Increasing amplitude can enhance or suppress transfer and produces a non-monotonic response in a representative sequence. In selected geometric comparisons, weaker transfer accompanies lower concentration variance and a mean shifted toward the high-concentration state. Concentration distributions and moment decomposition distinguish this mean shift from reduced spatial heterogeneity. These joint responses support a hydrodynamic shielding interpretation in which restricted trough-to-bulk exchange limits renewal of low-concentration near-wall fluid. The findings provide a physical basis for assessing how interface geometry regulates solute exchange and concentration redistribution in saline groundwater and geological carbon-storage systems.

1. Introduction

Buoyancy-driven solutal convection influences mass transfer in geological carbon storage and saline groundwater systems (De Paoli, 2023; Post et al., 2013). Theory, experiments and numerical studies of porous convection provide a basis for understanding instability, plume interaction and transport (Backhaus et al., 2011; De Paoli et al., 2024; Hewitt, 2020; Hewitt et al., 2012; Hidalgo et al., 2012; Zhu et al., 2024). A non-planar interface changes both the available exchange surface and the geometry of circulation. Greater relief may therefore alter the access of the overlying fluid to troughs as well as the total boundary flux. This raises two related questions: does increasing interface relief consistently enhance mass transfer, and does a change in transfer imply a corresponding change in concentration uniformity?

In these settings, dissolution fronts, thawing fronts and stratigraphic contacts can form non-planar interfaces. Fig. 1(a) shows the setup of our previous saltwater-over-permafrost experiments (Wang et al., 2025). Fingering morphology develops at low *Ra* (Fig. 1(b)), whereas a persistent wavy interface forms at high *Ra* (Fig. 1(c)). The associated local and larger-scale circulation patterns are illustrated schematically in Fig. 1(d, e), respectively. The persistent wavy morphology motivates the prescribed sinusoidal lower boundary used in the present study. The numerical problem examines flow and effective-scalar transport above this fixed boundary; it does not calculate thawing, dissolution or interface migration. This idealization separates the transport response to a given geometry from the evolution of the geometry itself.

The central question is how interface geometry changes porous-convective transfer and the associated concentration distribution. Existing studies have examined concentration boundary conditions (Amooie et al., 2018), permeability anisotropy (De Paoli et al., 2016), and the effects of pore structure and porosity on flow regimes (Li et al., 2025; Schwendener et al., 2026). Our related study examined geometry-dependent transfer, flow and dissipation, including transfer suppression associated with weakly ventilated troughs (Wang et al., 2026). The present study extends this line of inquiry by relating boundary transfer to mean concentration, segregation intensity and concentration PDFs. This comparison establishes whether apparent homogenization accompanies stronger exchange or a shift toward a

* Corresponding author.
E-mail address: jiansongwu@cumtb.edu.cn (J. Wu).

https://doi.org/10.1016/j.advwatres.2026.105522
Received 5 February 2026; Received in revised form 1 October 2026; Accepted 1 October 2026
Available online 2 October 2026
0309-1708/© 2026 Published by Elsevier Ltd.

boundary concentration, and places the shielding interpretation in the context of concentration redistribution.

Studies of wavy walls, grooved channels and internal obstacles show how boundary configuration changes circulation and transfer (Biswas et al., 2024; Mandal et al., 2026; Rahaman et al., 2024). Related work on complex cavities and annular or stepped geometries examines the response of circulation and transport to geometry and forcing (Hussain, 2025; Hussain et al., 2025, 2026; Manna et al., 2025). These studies provide context for geometric effects in systems with additional magnetic, rheological or nanoparticle physics. Here hydrodynamic shielding denotes restricted exchange between a trough and the overlying fluid. Fluid can circulate within a trough while exchange through its opening remains restricted. We therefore examine boundary flux together with concentration statistics to interpret the transport response.

We first examine how boundary transfer responds to wave count, amplitude and Rayleigh number, with particular attention to non-monotonic amplitude dependence. We then compare transfer with segregation intensity, mean concentration and concentration PDFs over the same observation windows. Their joint interpretation distinguishes changes in spatial spread from a shift toward a boundary concentration. Finally, we discuss whether hydrodynamic shielding offers a plausible explanation of these responses, separating the computed trends from the local exchange mechanism they suggest.

2. Materials and methods

The physical problem, governing equations, material properties and numerical method are described below, followed by the verification checks and the definitions used to compare boundary transfer with the concentration field.

2.1. Physical problem, geometry and assumptions

Fig. 2 shows the wavy-boundary configuration and the flat-boundary reference considered in this study. We consider a two-dimensional, homogeneous porous layer containing a single fluid with density increasing linearly with an effective concentration variable. A prescribed sinusoidal lower boundary is held at a lower reference concentration than the upper boundary, placing lighter fluid below denser fluid. The interface morphology observed in saltwater-over-permafrost experiments motivates the geometry (Wang et al., 2025). The calculation holds that geometry fixed and uses the concentration transport equation in Section 2.2. It does not predict thawing, dissolution kinetics

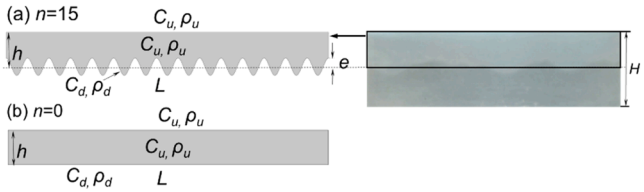

Fig. 2. Geometric model: (a) wavy lower boundary and (b) flat lower boundary. The upper and lower reference concentrations, labelled C_u and C_d, correspond to $c = 1$ and $c = 0$, respectively. The fixed wavy interface is $y = e[\cos(2\pi nx/L) - 1]$, the upper boundary is $y = 15$ mm, and $L = 60\pi$ mm.

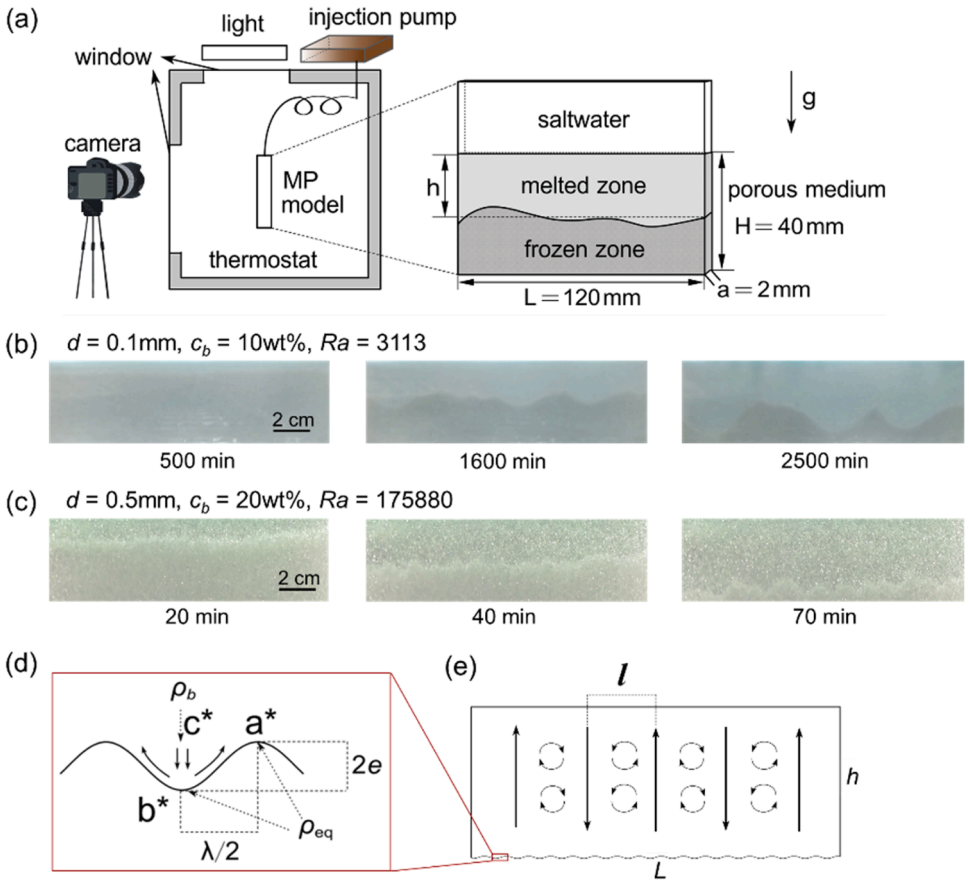

Fig. 1. Experimental motivation for the fixed wavy interface (Wang et al., 2025). (a) Setup for visualizing permafrost thawing beneath saltwater. (b) Fingering morphology at low *Ra* and (*c*) a persistent wavy morphology at high *Ra* in those experiments. (d) Schematic of local circulation from crest a* toward trough b* associated with the fingering regime. (*e*) Schematic of larger-scale Rayleigh–Darcy convection associated with the wavy regime. These experimental observations motivate the prescribed geometry; front evolution and its stabilization are not simulated in the present study.

or the evolution of a specific solute.

The computational domain is defined in Cartesian coordinates (x, y), with horizontal width $L = 60\pi$ mm and upper boundary $y = 15$ mm. A fixed reference length $h' = 20$ mm is used for nondimensionalization; the physical layer depth follows from the prescribed upper and lower boundaries. The porous medium is homogeneous and isotropic, and the pore fluid is incompressible; all properties are constant except for the density variation retained in the buoyancy term under the Boussinesq approximation.

The lower boundary is prescribed as a sinusoidal surface $y_b(x) = e\left[cos\left(\frac{2\pi nx}{L}\right) - 1\right]$, where e is the wave amplitude and n is the number of waves across the domain. The geometric combinations in Table 1 use $n = 5$, 10 and 15 and $e = 2$, 4 and 6 mm, corresponding to $e/h' = 0.10$, 0.20 and 0.30. The analysis comprises 99 cases at $Ra = 1$, 10, 60, 100, 300, 500, 1000, 3000, 5000, 10,000 and 20,000. All nine geometries are represented at each Ra.

2.2. Governing equations and boundary conditions

2.2.1. Dimensional governing equations, initial and boundary conditions

We consider incompressible, laminar buoyancy-driven flow in a homogeneous isotropic porous medium. Continuity and the transient Darcy–Brinkman momentum balance govern the superficial velocity u. Normalized effective concentration is defined through the assumed linear density–concentration relation as $c = \frac{\rho - 1053\ \mathrm{kg/m^3}}{56\ \mathrm{kg/m^3}}$. Thus $c = 0$ and $c = 1$ correspond to the low- and high-concentration reference states of the same fluid, with densities 1053 and 1109 kg/m^3. Density variations act through buoyancy under the Boussinesq approximation. The density-based normalization does not specify absolute molar concentrations or identify a particular solute without an independent concentration calibration.

The Darcy–Brinkman formulation retains viscous momentum diffusion alongside resistance from the porous matrix and permits a no-slip condition at the wavy wall. Brinkman boundary effects have been analysed for convection onset in porous layers (Rees, 2002), while coupled Stokes–Brinkman–Darcy models describe momentum exchange at fluid–porous interfaces (Ruan and Rybak, 2025, 2026). Here the formulation is used throughout the homogeneous porous layer to represent velocity gradients near the prescribed wall. The low Reynolds numbers support neglect of nonlinear advective inertia, while unsteady inertia is retained. The analysis is conducted within this continuum model; the cited studies provide its modelling context rather than validation of the present geometry.

$$\frac{\rho_0}{\varphi}\frac{\partial \boldsymbol{u}}{\partial t} + \frac{\mu}{K}\boldsymbol{u} = -\nabla p + \mu_{\mathrm{eff}}\nabla^2\boldsymbol{u} + (\rho - \rho_{\mathrm{ref}})\boldsymbol{g} \tag{1}$$

The flow satisfies $\nabla\cdot u = 0$ and Eq. (1), where K is permeability, μ is dynamic viscosity, $\rho_0 = 1109$ kg/m^3 and $\rho_{\mathrm{ref}} = 1053$ kg/m^3. The gravity vector $\boldsymbol{g}$ points downwards and has magnitude g. $\rho - \rho_{\mathrm{ref}} = \Delta\rho c$, with $\Delta\rho = 56$ kg/m^3. The effective viscosity is $\mu_{\mathrm{eff}} = \mu/\varphi$.

$$\varphi\frac{\partial c}{\partial t} + \boldsymbol{u}\cdot\nabla c = D\nabla^2 c \tag{2}$$

Transport of the normalized concentration is governed by the advection–diffusion Eq. (2), where $\varphi = 0.42$ is the porosity, u is the superficial velocity and $D = 2.29 \times 10^{-9}$ m^2/s is the diffusion coefficient. No volumetric solute source or sink is included.

The prescribed initial state is $c = 1$. The upper boundary has $c = 1$ and an open-boundary normal-stress condition, with prescribed normal stress $f_0 = 0$ and hydrostatic compensation enabled. In the wavy models, flow and concentration are periodic on the same lateral boundary pair, with zero prescribed pressure and concentration differences.

2.2.2. Dimensionless governing equations, initial and boundary conditions

For nondimensionalization, the fixed reference length h' and diffusion coefficient D define the time, velocity and pressure scales h'^2/D, D/h' and $\mu D/K$, respectively. Thus $x^* = x/h'$, $y^* = y/h'$, $t^* = \frac{tD}{h'^2}$, $u^* = \frac{uh'}{D}$ and $p^* = \frac{pK}{\mu D}$; c is already dimensionless.

With this scaling, the dimensionless governing system is

$$\nabla\cdot u^* = 0 \tag{3}$$

$$\frac{Da}{\varphi Sc}\frac{\partial \boldsymbol{u}^*}{\partial t^*} + \boldsymbol{u}^* = -\nabla p^* + \frac{Da}{\varphi}\nabla^2\boldsymbol{u}^* + \varphi Ra c\mathbf{e}_y \tag{4}$$

$$\varphi\frac{\partial c}{\partial t^*} + u^*\cdot\nabla c = \nabla^2 c \tag{5}$$

Here $Ra = \frac{\Delta\rho g K h'}{\varphi\mu D}$, $Da = \frac{K}{h'^2}$, and $Sc = \frac{\mu}{\rho_0 D}$. In Eqs. (3)–(5), ∇ denotes differentiation with respect to the dimensionless coordinates. The scalar boundary values remain $c = 0$ below and $c = 1$ above, with lateral periodicity. The unit vector $\mathbf{e}_y$ in Eq. (4) specifies the downward gravity direction.

2.3. Physical properties and parameter space

The fixed material parameters are $\mu = 1.792 \times 10^{-3}$ Pa s, $\varphi = 0.42$ and $D = 2.29 \times 10^{-9}$ m^2/s. Porosity and permeability are motivated by the glass-bead saline system of Wang et al. (2025). With $\rho_0 = 1109$ kg/m^3 and $h' = 0.020$ m, $Sc = 705.62$ and $Da = 7.84, 625 \times 10^{-8}$. Table 2 gives $u_b = K\Delta\rho g/\mu$ and $Re = \rho_0 u_b\sqrt{K}/\mu$; the largest Re is 3.335×10^{-3}.

2.4. Numerical implementation and post-processing

The governing equations were solved in COMSOL Multiphysics 6.1.0.252 using quadratic Lagrange elements for velocity and concentration and linear elements for pressure. The fully coupled solver uses

Table 2
Characteristic buoyancy velocity u_b, Rayleigh-Darcy number Ra and Reynolds number Re used in this study.

u_b (m/s)	Ra	Re
4.809×10^{-8}	1	1.667×10^{-7}
4.809×10^{-7}	10	1.667×10^{-6}
2.885×10^{-6}	60	1×10^{-5}
4.809×10^{-6}	100	1.667×10^{-5}
1.443×10^{-5}	300	5.002×10^{-5}
2.405×10^{-5}	500	8.336×10^{-5}
4.809×10^{-5}	1000	1.667×10^{-4}
1.443×10^{-4}	3000	5.002×10^{-4}
2.405×10^{-4}	5000	8.336×10^{-4}
4.809×10^{-4}	10,000	1.667×10^{-3}
9.618×10^{-4}	20,000	3.335×10^{-3}

Table 1
Geometric combinations represented in the dataset.

Case ID	G1	G2	G3	G4	G5	G6	G7	G8	G9
n	5	5	5	10	10	10	15	15	15
$\lambda = L/n$ (mm)	37.70	37.70	37.70	18.85	18.85	18.85	12.57	12.57	12.57
e (mm)	2	4	6	2	4	6	2	4	6
e/h'	0.10	0.20	0.30	0.10	0.20	0.30	0.10	0.20	0.30

PARDISO. Scalar streamline and crosswind stabilization are enabled, while isotropic artificial diffusion is disabled. Fifteen boundary-layer mesh rows refine the wavy lower interface, with nominal first thickness 2 μm and growth factor 1.15, giving a total thickness of 95.16 μm. The mesh and time-step comparisons are reported in Section 2.5. Time integration uses adaptive implicit backward differentiation formulas of orders 1–2 with relative tolerance 0.005. Stored output times differ from internal solver steps. Domain statistics and boundary fluxes are evaluated by native area and boundary integration.

The Sherwood number is defined by $Sh = \frac{h'}{DL}\int_{\Gamma_b} J_c \cdot n ds$ where $J_c = uc - D\nabla c$ is the flux of normalized effective concentration and n is the outward unit normal of the fluid domain. Positive Sh denotes effective-scalar transfer out of the fluid through the lower, low-concentration boundary. At this no-slip boundary the flux is diffusive; the boundary condition does not inject fluid into the domain. The integration follows the actual wavy interface Γ_b, while normalization uses its horizontal projection L. Sh therefore measures interface scalar transfer per horizontal footprint and includes the effects of both geometry and convective redistribution near the interface.

The intensity of segregation is $I = 4\langle (c - \langle c \rangle)^2 \rangle$, where angle brackets denote an area average over the fluid domain. The reference variance 0.25 is the maximum for concentrations confined to [0, 1], attained when equal areas have $c = 0$ and $c = 1$. I measures spatial concentration heterogeneity. To determine whether a lower I accompanies a change in mean concentration, we also evaluate the mean-composition bias $B = (2\langle c \rangle - 1)^2$ and the complementary second moment $M = 4\langle c(1 - c) \rangle$; these satisfy $I + B + M = 1$ at every saved time. B measures the magnitude of the mean's displacement from the midpoint $c = 0.5$; its direction is identified from the mean concentration and PDF. Neither I nor B measures a molecular mixing rate.

2.5. Validation and numerical sensitivity

Grid-sensitivity study. Nine mesh levels, from 4385 to 243,738 elements, were compared for $n = 15$, $e = 6$ mm and $Ra = 20{,}000$ (Table 3). The Normal test mesh gives $Sh = 197.055$, compared with 197.901 on the finest mesh, a difference of 0.43%. The change from the Normal to the next finer mesh is 0.52%, and all five levels from Normal to Extremely fine differ from the finest result by at most 1.21%. These comparisons support the Normal mesh as an economical choice for the mean Sh in this representative test. The small, non-monotonic differences among the finer meshes can arise because refinement changes local boundary resolution, the representation of the curved wall and the evaluation of wall gradients; finite-time averaging of fluctuating convection can also contribute.

Time-step-sensitivity study. Production calculations use automatic maximum-step selection. For $n = 15$ and $e = 6$ mm, Table 4 compares the reported reference means Sh_{s1}, obtained with a 1 s maximum internal step, with the automatic-setting means Sh_{s2}. Relative differences are 0.56–4.32%. Both solver settings are adaptive; the cap is distinct from a fixed step or a saved-output interval. These comparisons show that changing the maximum-step setting has a limited effect on the reported mean Sh: the largest difference is 4.32%, and the differences at $Ra = 10{,}000$ and 20,000 are below 0.9%. The automatic setting is therefore supported for comparing mean boundary transfer over the tested Ra range at this geometry, with the sensitivity quantified in Table 4.

Table 3
Nine-level mesh-sensitivity study for $n = 15$, $e = 6$ mm and $Ra = 20{,}000$.

Mesh level	Elements	Sh	Difference to finest (%)	Difference to next finer (%)
Extremely coarse	4385	1.83	99.08	98.90
Ultra coarse	6030	166.58	15.83	3.86
Coarser	8116	160.39	18.95	14.88
Coarse	12,039	188.43	4.79	4.38
Normal	18,115	197.055	0.43	0.52
Fine	20,939	198.080	0.09	1.11
Finer	28,958	200.297	1.21	1.61
Ultra-fine	50,057	197.114	0.40	0.40
Extremely fine	243,738	197.901	—	—

Table 4
Maximum-internal-step sensitivity for $n = 15$ and $e = 6$ mm. Sh_{s1} denotes the mean Sh with a 1 s maximum internal step; Sh_{s2} denotes the mean Sh with automatic maximum-step selection. Relative difference is $100 \times |Sh_{s2} - Sh_{s1}|/|Sh_{s1}|$.

Ra	Sh_{s1}	Sh_{s2}	Relative difference (%)
1000	26.81	27.39343	2.18
3000	57.38	59.85904	4.32
5000	69.34	71.54327	3.18
10,000	118.65	117.98407	0.56
20,000	195.39	197.05499	0.85

Diffusion-limit comparison. The diffusion reference is obtained by setting the velocity and source to zero and solving Laplace's equation with $c = 0$ below and $c = 1$ above. For this theoretical comparison, place the mean lower wall at $y = 0$ and the top at $y = h$, with $h = h' = 20$ mm and $h/h' = 1$. The lower wall is $y = e\cos(k_w x)$, where $k_w = 2\pi n/L$. At fixed h and k_w, seek $c = c_0 + e\,c_1 + e^2 c_2 + O(e^3)$.

$$c = c_0 + ec_1 + e^2 c_2 + O(e^3),\ c_0 = \frac{y}{h} \tag{6}$$

The leading solution is $c_0 = y/h$. Taylor expansion of the lower Dirichlet condition about $y = 0$ gives $c_1(x,0) = -\cos(k_w x)/h$ and $c_2(x,0) = -\cos(k_w x)\partial c_1(x,0)/\partial y$. Both corrections vanish at $y = h$. Solving the resulting harmonic boundary-value problems gives the expressions below.

$$c_1 = -\frac{\cos(k_w x)\sinh(k_w(h - y))}{h\sinh(k_w h)} \tag{7}$$

$$c_2 = -\frac{k_w \coth(k_w h)}{2h}\left[\frac{h - y}{h} + \cos(2k_w x)\frac{\sinh(2k_w(h - y))}{\sinh(2k_w h)}\right] \tag{8}$$

Both correction fields satisfy Laplace's equation. Their upper boundary values vanish. At the lower boundary, the $O(e)$ and $O(e^2)$ terms in the Taylor-expanded Dirichlet condition cancel separately. These six residual checks are evaluated symbolically and are zero. No coefficient is fitted to the COMSOL results.

Only the horizontally averaged part of c_2 contributes to the integrated top diffusive flux. Because the stationary zero-source diffusive flux balances between the two walls, the projected lower-wall Sherwood number follows as $Sh_{\mathrm{diff}} \approx \frac{h'}{h}\left[1 + \frac{e^2 k_w \coth(k_w h)}{2h}\right]$. For the Table 5 calculation, $h/h' = 1$ and $h = h' = 20$ mm, so the prefactor h'/h equals one. The fixed reference length h' is the one used to normalize the numerical Sh.

The small parameters in the expansion are e/h and $k_w e$. For $e = 2$ mm

Table 5
Independent low-Ra validation for $e = 2$ mm and $h = 20$ mm. Numerical Sh is the recovered lower-boundary flux from the independent $Ra = 1$ validation solutions, normalized by projected width as in Section 2.4. Weak-wave Sh is the second-order, zero-flow, source-free diffusion approximation in Section 2.5, with the same normalization. Difference (%) is 100 × (Numerical Sh − Weak-wave Sh)/Weak-wave Sh.

n	$k_w e$	Numerical Sh	Weak-wave Sh	Difference (%)
5	0.333	1.016373	1.016709	−0.033
10	0.667	1.030471	1.033333	−0.277
15	1.000	1.041348	1.050000	−0.824

and $h = 20$ mm, $e/h = 0.1$ and k_w $e = 0.3333$, 0.6667 and 1.0000 at $n = 5$, 10 and 15, respectively. The $n = 5$ case lies closest to a weak-slope limit; $n = 15$ is not a small-slope case. Results at larger amplitudes are not used to claim asymptotic accuracy.

For $e = 2$ mm, $h = h' = 20$ mm and $L = 60\pi$ mm, the expression gives $Sh = 1.016709$, 1.033333 and 1.050000 at $n = 5$, 10 and 15, respectively. The signed differences for the independent validation solutions in Table 5 are −0.033%, −0.277% and −0.824%, using 100 × (Numerical Sh − Weak-wave Sh)/Weak-wave Sh. Both series increase with n, with the closest agreement at $n = 5$. This comparison provides a low-Ra diffusion reference. It is not a linear-stability calculation, and finite $Ra = 1$ is not the exact zero-flow limit; the comparison does not validate high-Ra plume exchange or hydrodynamic shielding.

3. Results and discussion

A wavy boundary regulates both boundary transfer and concentration redistribution within the porous layer. We compare Sh, concentration variance, mean concentration and PDFs over common late-time windows to establish their joint dependence on Rayleigh number and geometry. The analysis first identifies the transfer enhancement accompanying developing convection and the geometric constraints on relative transfer gains in the vigorous-convection range. Concentration statistics then reveal whether the accompanying redistribution involves a narrower concentration distribution, a shift of its mean, or both. These linked observations provide the basis for interpreting transfer suppression through hydrodynamic shielding.

3.1. Transient evolution and averaging windows

Fig. 3 shows the transient evolution of boundary transport and mean concentration for $n = 5$, $e = 2$ mm and $Ra = 5000$. These histories provide the basis for examining the late-time interval used in the comparisons. Solute loss through the lower $c = 0$ wall initially establishes a lighter region beneath the denser initial fluid. This unstable density stratification drives convection, coupling flow and solute transport. Over 5000–10,000 s, the mean lower-wall Sh is 74.32. The upper and lower curves use different flux evaluations and do not establish a steady through-flux. The concentration history is therefore considered together with the transport history when interpreting the selected interval.

Here, quasi-steady behavior is characterized by late-time statistics after the initial development of convection; instantaneous fluxes and concentration may continue to fluctuate. For each case, t_s denotes the beginning of the adopted averaging interval and t_{end} the final saved time. A reported time mean is the time integral of the quantity over this interval divided by $t_{end} - t_s$. In Fig. 3, $t_s = 5000$ s and $t_{end} = 10{,}000$ s. The subsequent comparisons of Sh, mean concentration, I, B, M and the concentration PDFs use the primary interval listed for each case in Table 6. The moments are evaluated from the instantaneous spatial field before time averaging. Shorter late-time windows provide the sensitivity spans shown in the figures. This common averaging procedure separates the reported response from individual peaks and troughs in the transient histories.

Table 6
Common time range and three observation windows for each Ra.

Ra	Cases	Common start (s)	Common end (s)	50% window start (s)	75% window start (s)	90% window start (s)
1	9	0	800,000	400,000	600,000	720,000
10	9	0	800,000	400,000	600,000	720,000
60	9	0	600,000	300,000	450,000	540,000
100	9	0	30,000	15,000	22,500	27,000
300	9	0	200,000	100,000	150,000	180,000
500	9	0	200,000	100,000	150,000	180,000
1000	9	0	30,000	15,000	22,500	27,000
3000	9	0	20,000	10,000	15,000	18,000
5000	9	0	10,000	5000	7500	9000
10,000	9	0	10,000	5000	7500	9000
20,000	9	0	5000	2500	3750	4500

The dataset contains 99 revised wavy cases covering nine geometries at eleven Ra values. Table 6 gives the common observation intervals. For a given Ra, the common interval is the intersection of the native saved-field time ranges across the available geometries. Its final half defines the primary window, and its final quarter and final tenth define two distinct sensitivity windows. Some dense probe histories retain only a late portion of a simulation. They are therefore used for cross-checks over the available overlap, with identical endpoints for the native and probe integrals and an explicit overlap fraction. Their truncation does not shorten the field-based observation windows. A late interval is not, by itself, evidence of statistical stationarity.

3.2. Non-monotonic mass transfer and geometric dependence

To determine how boundary geometry affects mass transfer as Ra varies, we compare Sh/Ra at each fixed amplitude, using the flat layer as a common reference. Comparisons among wave counts identify the effect of wavelength, while the amplitude sequence quantifies enhancement and suppression as boundary relief increases.

The flat layer provides a reference alongside the flat-boundary studies of Hewitt et al. (2012) and Zhu et al. (2024). It has thickness 20 mm and the same width $L = 60\pi$ mm and reference length $h' = 20$ mm used here. Sh approaches unity at low Ra, while Sh/Ra varies less at high Ra.

The discussion uses three comparison ranges based on the classical flat-layer reference of Hewitt et al. (2012): $Ra \langle 4\pi^2$, $4\pi^2 \leq Ra \leq 1300$ and $Ra \rangle 1300$. These bounds organize the geometric comparisons rather

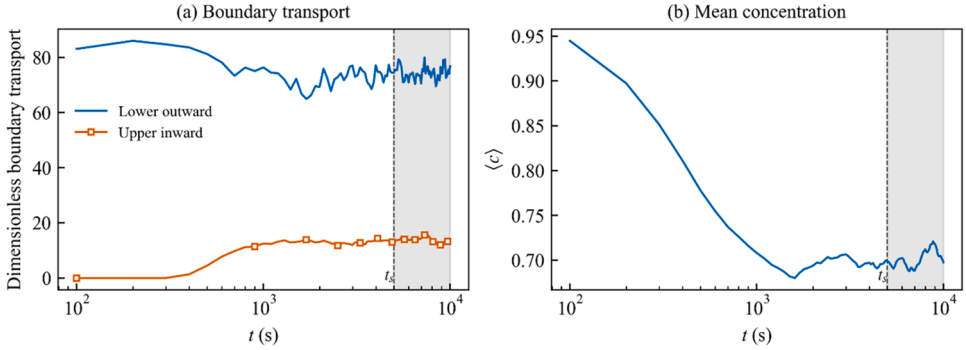

Fig. 3. Boundary transport and mean concentration for $n = 5$, $e = 2$ mm and $Ra = 5000$. (a) Recovered lower-wall Sh (positive outward) and direct-gradient plus advective upper-boundary transport (positive inward), expressed on the same dimensionless scale. The ordinate is dimensionless boundary transport, rather than a dimensional flux. (b) Area-mean concentration. Dashed vertical lines mark the start of averaging, $t_s = 5000$ s; shading extends to the final time, $t_{end} = 10{,}000$ s.

than define newly determined stability thresholds for the wavy layers. We examine diffusive transfer, the development of convection, and transfer differences under vigorous convection in turn. Wave count n and amplitude e describe the frequency and magnitude of the boundary undulations, respectively, and their effects are compared separately.

(1) Diffusion-dominated range ($Ra < 4\pi^2$): the wavy geometry changes the background level of diffusive transfer. In Fig. 4, *Sh*/*Ra* varies approximately inversely with *Ra*, corresponding to nearly unchanged *Sh* at $Ra = 1$ and 10. *Sh* for the wavy layers is slightly above the flat-layer reference, indicating a modest transfer enhancement for these geometries. Among the wavy layers, increasing n at fixed e slightly raises *Sh*, whereas increasing e at fixed n lowers *Sh*. These results establish contrasting effects of wave count and amplitude on diffusive transfer at low *Ra*.

(2) Transition range ($4\pi^2 \leq Ra \leq 1300$): developing convection enhances transfer, while geometry changes the magnitude of the enhancement. The curves depart from the inverse dependence at low *Ra* and separate and cross more clearly. *Sh* exceeds its low-*Ra* level, but its dependence on n varies with both *Ra* and e. For example, at $Ra = 1000$, the largest *Sh* occurs at $n = 10$ for $e = 2$ mm, but at $n = 15$ for $e = 4$ and 6 mm. As *Ra* increases through the transition range, convection develops and enhances transfer, with the gain depending on boundary wavelength.

(3) Vigorous-convection range ($Ra > 1300$): geometry limits the transfer gain. *Sh*/*Ra* for the flat-layer reference approaches an approximately constant value, whereas the wavy-layer curves generally continue to decline over the sampled $Ra = 3000$–$20{,}000$ range and lie below the flat reference at high *Ra*. This decline concerns *Sh*/*Ra*; *Sh* itself still increases with *Ra*. The increase in *Sh* is therefore generally less than proportional to the increase in *Ra* over this range. Geometric differences are especially clear at $e = 6$ mm, where *Sh* at $n = 15$ exceeds that at $n = 5$ throughout this range; the ordering is less consistent at smaller amplitudes. Together with the non-monotonic amplitude sequence in Fig. 4(d), these results identify the combined wave count and amplitude as controls on transfer enhancement and suppression under vigorous convection.

At $Ra = 10{,}000$, increasing e from 2 to 6 mm reduces *Sh* by 45.6% at $n = 5$, but raises it by 16.0% at $n = 15$. Together with the non-monotonic sequence at $Ra = 5000$, these comparisons demonstrate amplitude-dependent enhancement and suppression controlled by wave count. The reduction at $n = 5$ remains when each geometry is normalized by its own $Ra = 1$ transfer: the gains are 88.34 and 53.41 for $e = 2$ and 6 mm, respectively. This comparison accounts for their different low-*Ra* transfer levels, but $Ra = 1$ is not an exact zero-flow reference and does not isolate wall-area effects. The transfer comparisons establish geometry-dependent enhancement and suppression. We next relate these responses to changes in mean concentration and spatial spread, providing the concentration evidence needed to assess a hydrodynamic shielding interpretation.

3.3. Segregation metric *I* and concentration heterogeneity

To quantify spatial concentration heterogeneity, we calculate the intensity of segregation I as defined in Section 2.4: four times the area-weighted concentration variance, averaged over the same late-time windows. A larger I indicates a more heterogeneous concentration field, whereas a smaller I indicates a more uniform field. Fig. 5 uses the three *Ra* ranges in Section 3.2 to compare how this heterogeneity varies with *Ra* and boundary geometry.

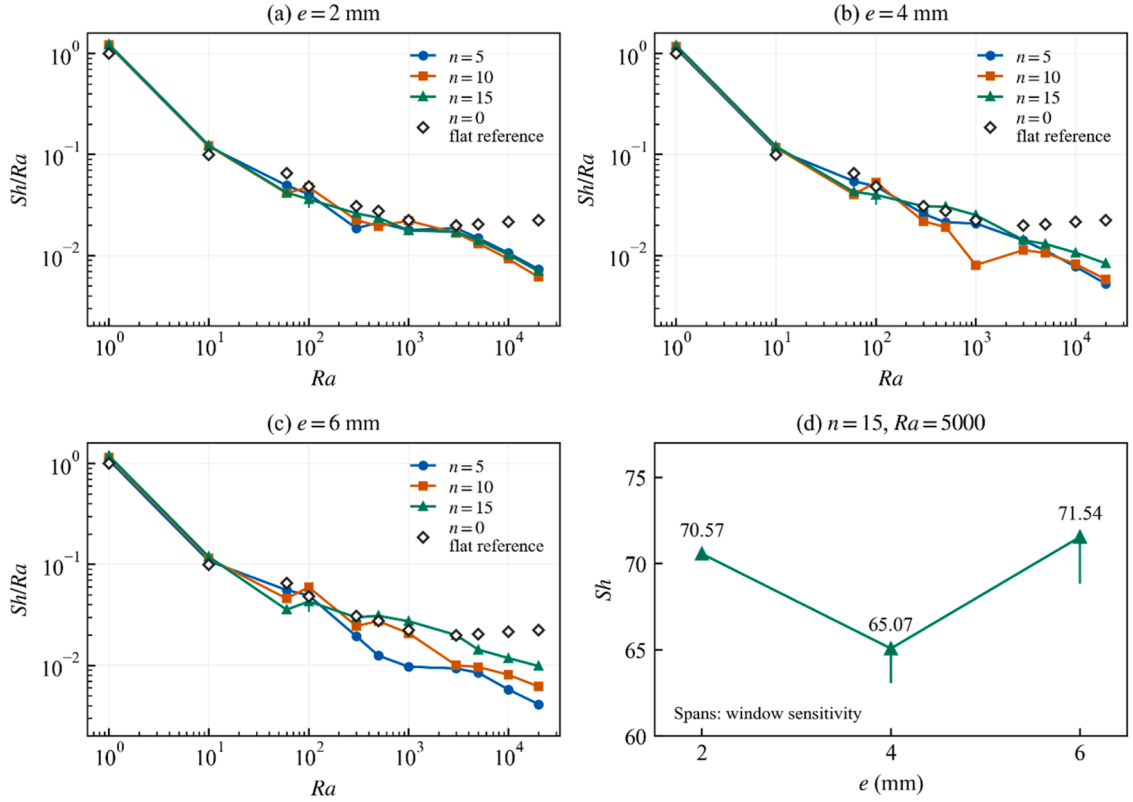

Fig. 4. Boundary-transfer statistics. (a–c) *Sh*/*Ra* versus *Ra* at $e = 2$, 4 and 6 mm, with common axis limits. Colored symbols identify $n = 5$, 10 and 15; black hollow diamonds show the same 20 mm flat-layer reference in each panel. (d) The $n = 15$, $Ra = 5000$ amplitude sequence. Vertical spans show the range across three observation windows.

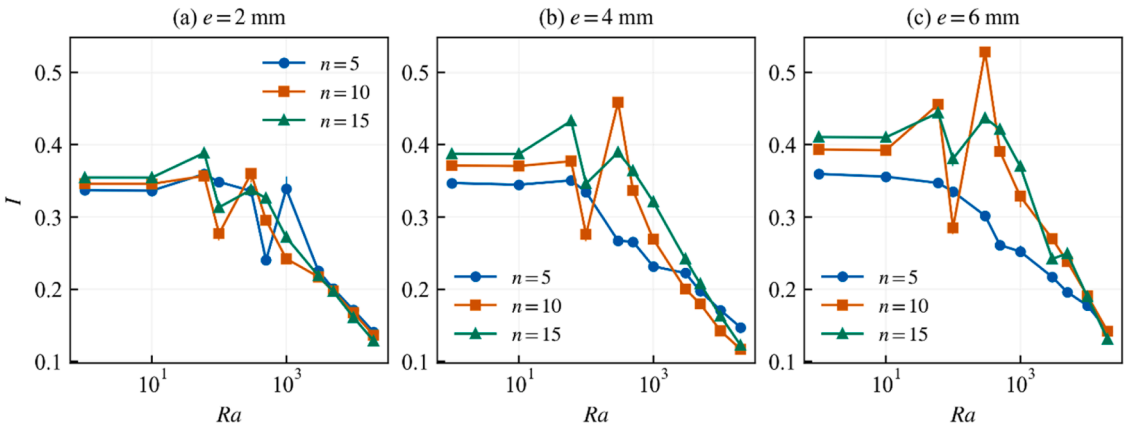

Fig. 5. Intensity of segregation I versus Ra for the wavy geometries. Panels (a–c) correspond to e = 2, 4 and 6 mm, with the same vertical scale. Colored symbols and window-sensitivity spans are as in Fig. 4.

(1) Diffusion-dominated range ($Ra < 4\pi^2$): stronger boundary undulations make the concentration field more heterogeneous. I changes little as Ra rises from 1 to 10; it increases with n at fixed e and with e at fixed n. Increasing either wave count or amplitude therefore increases spatial concentration differences in this diffusion-dominated range. Together with Fig. 4, this shows that geometry can change the concentration profile while overall transfer remains close to its respective diffusive background level.

(2) Transition range ($4\pi^2 \leq Ra \leq 1300$): concentration heterogeneity changes non-monotonically as convection develops. The I curves separate, cross and exhibit peaks that depend on geometry. For example, as Ra rises from 100 to 300, I increases for $n = 10$ at all amplitudes, indicating greater heterogeneity, whereas it decreases for $n = 5$, indicating greater uniformity. Enhanced convective transfer thus accompanies different patterns of concentration redistribution across geometries. Geometry-dependent circulation and plume structures redistribute concentration, accompanying the different transfer gains in Fig. 4.

(3) Vigorous-convection range ($Ra > 1300$): concentration becomes more uniform overall, while boundary transfer remains sensitive to geometry. For all nine geometries, I is lower at $Ra = 20{,}000$ than at $Ra = 3000$, and the spread among geometries narrows, although the individual curves are not strictly monotonic. Spatial concentration differences therefore generally decrease as Ra increases across this range. At the same time, Sh remains strongly dependent on geometry. Table 7 further shows that, in selected amplitude comparisons, lower I can coexist with lower Sh and a higher mean concentration. The state toward which the concentration shifts must therefore be examined alongside its spatial uniformity.

Table 7 compares Sh, I and mean concentration for two amplitude pairs at $Ra = 10{,}000$. Both show lower computed Sh and a higher mean as amplitude increases. The $n = 10$ pair illustrates why a reduction in variance must be interpreted with the mean; the $n = 5$ pair shows a much smaller variance change.

Table 7
Two illustrative amplitude comparisons at $Ra = 10{,}000$. Instantaneous I and B are averaged after evaluation.

n	e (mm)	Sh	I	$\langle c \rangle$	B
10	2	92.28	0.1674	0.7315	0.2149
10	4	82.32	0.1427	0.7878	0.3314
5	2	105.95	0.1713	0.7227	0.1986
5	6	57.68	0.1775	0.7455	0.2413

(1) **Reduced transfer with lower concentration variance**
At $n = 10$, increasing e from 2 to 4 mm reduces Sh by 10.8% and I by 14.8%, while mean concentration rises from 0.7315 to 0.7878 (Table 7). The computed concentration field is more uniform, but also closer to the high-concentration upper-boundary state. Thus, a reduction in concentration variance can accompany weaker boundary transfer when more of the domain approaches the high-concentration state.

(2) **Reduced transfer with a small variance change**
At $n = 5$, increasing e from 2 to 6 mm lowers Sh while I increases by 3.63% and mean concentration rises (Table 7). The change in I is small, and this pair uses a different amplitude increment from the $n = 10$ pair. We therefore emphasize the common response of the two comparisons: mean concentration rises as boundary transfer weakens. This shared shift provides the basis for interpreting the composition change accompanying transfer suppression. The variance response adds complementary information about the geometry-dependent spatial distribution.

3.4. Probability-density interpretation of concentration states

To interpret the variance trends, we examine area-weighted concentration probability density functions (PDFs), averaged over the same windows as the other statistics. A PDF describes how the domain area is distributed over concentration: its integral over a concentration interval gives the fraction of the total area within that interval. For the histograms used here, each bin density equals its area fraction divided by the bin width, 0.025. Figs. 6 and 7 compare the effects of Rayleigh number, amplitude and wave count.

(1) Diffusion-dominated range ($Ra < 4\pi^2$): geometry changes a broadly distributed concentration profile. At $Ra = 1$ and 10, the PDFs in Fig. 6 remain broad and vary little with Ra. Increasing e raises the weight at low concentrations and lowers the mean, while the increase in I indicates greater concentration heterogeneity. Geometric effects in this range therefore mainly redistribute the diffusive profile, consistent with the weak dependence of Sh on Ra.

(2) Transition range ($4\pi^2 \leq Ra \leq 1300$): enhanced transfer accompanies a shift of the concentration distribution toward higher concentrations. A pronounced peak develops near $c = 1$, while the intermediate-concentration part also changes substantially. For $e = 2$ and 4 mm, the last-bin peak reaches its sampled maximum at $Ra = 300$; for $e = 6$ mm, it peaks at $Ra = 500$. All then decrease by $Ra = 1000$. Developing convection thus changes both boundary exchange and the area fractions occupied by

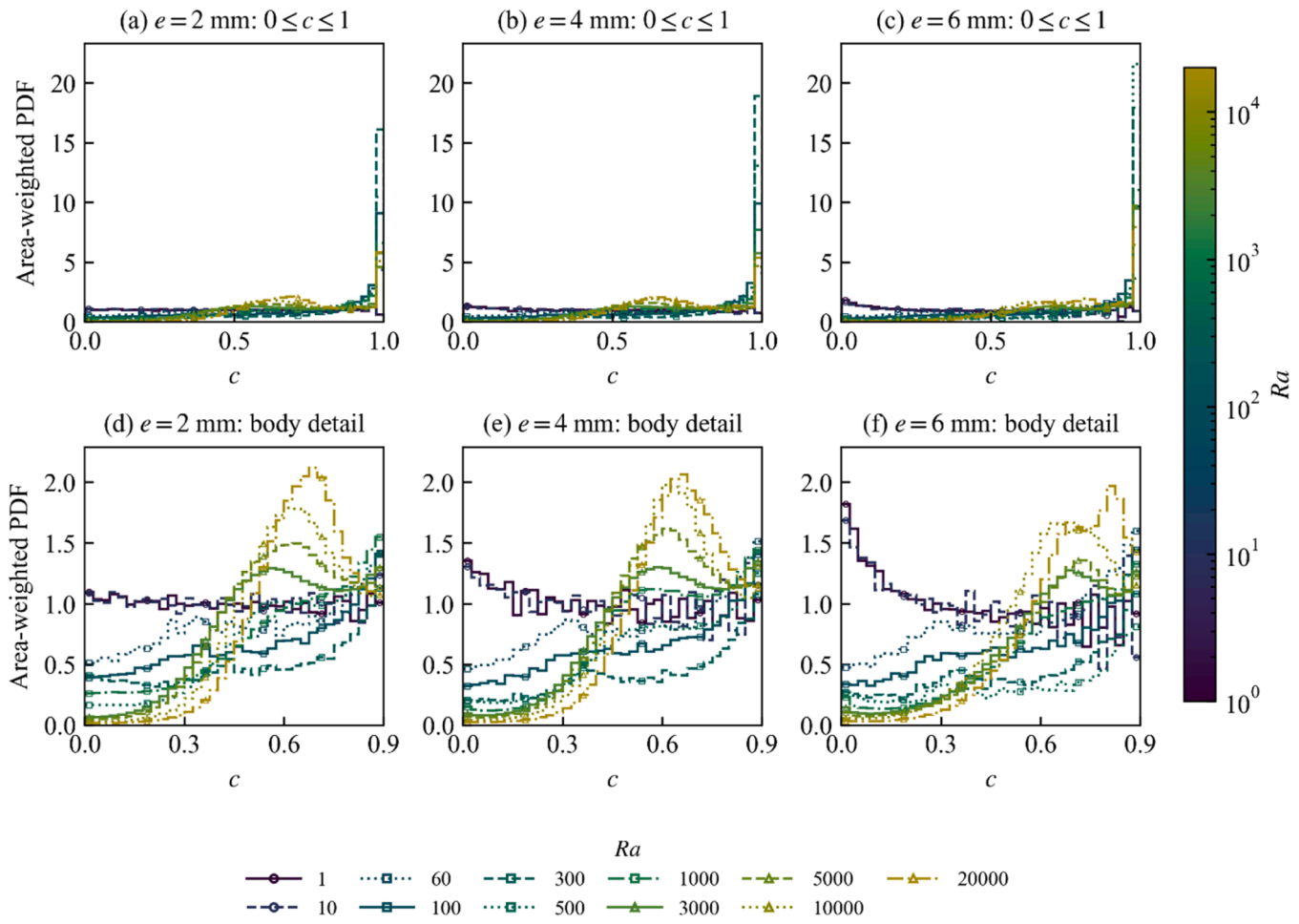

Fig. 6. Area-weighted concentration PDFs for $n = 5$. Panels (a–c) show $0 \le c \le 1$ at $e = 2$, 4 and 6 mm; panels (d–f) show $0 \le c \le 0.9$ on an expanded common vertical scale. All peak bins remain visible in the upper row. Color denotes Ra on a logarithmic scale; the legend identifies each curve by color, line style and marker. Hollow circles, squares and triangles distinguish $Ra \langle 4\pi^2$, $4\pi^2 \le Ra \le 1300$ and $Ra \rangle 1300$, respectively, at every seventh bin. The cumulative distribution function (CDF) is the fraction of total domain area with concentration at or below a given value. Differences between CDF values at adjacent bin edges give the area fractions in bins of width 0.025; division by this width gives the plotted PDF, averaged over the primary window for each Ra. Both rows retain full-domain normalization.

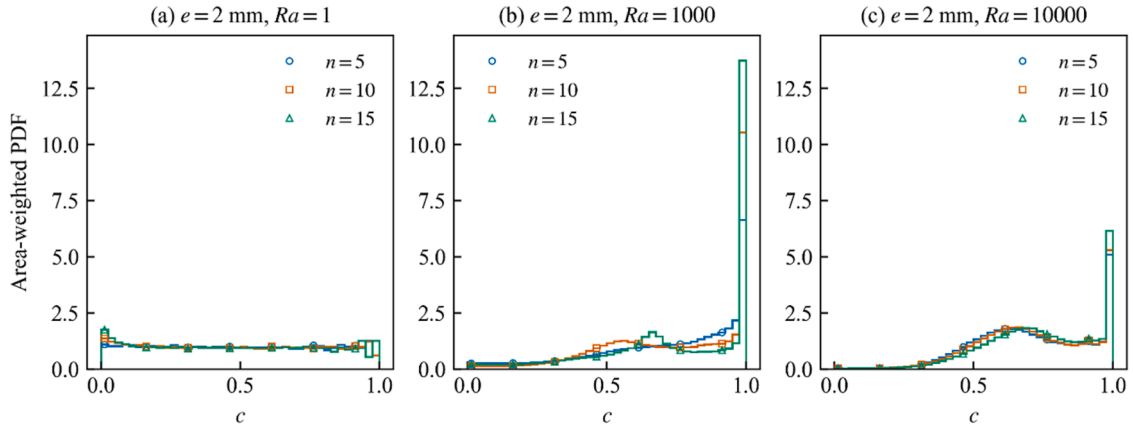

Fig. 7. Direct concentration-PDF comparisons at fixed $e = 2$ mm. Panels (a–c) show $Ra = 1$, 1000 and 10,000 with a common vertical scale. Circles, squares and triangles identify $n = 5$, 10 and 15; markers appear at every sixth bin. Each panel uses identical observation-window endpoints across the three geometries. Bin width, area weighting and treatment of out-of-range values follow Fig. 6.

different concentrations. The varying high-concentration peak and the non-monotonic response of I describe this redistribution.

(3) Vigorous-convection range ($Ra > 1300$): the concentration field is more uniform, but the high-concentration state retains substantial weight. The peak near $c = 1$ persists alongside a broad intermediate-concentration distribution. For $e = 2$ and 4 mm, the area fraction within $0.3 < c \le 0.8$ increases from about 0.52–0.53 at $Ra = 3000$ to about 0.59 at $Ra = 20{,}000$; the change is less

regular at $e = 6$ mm. The overall reduction in heterogeneity indicated by I thus occurs alongside persistent intermediate- and high-concentration regions. The coexistence of intermediate- and high-concentration regions helps explain why a more uniform field can still accompany weaker boundary transfer.

Fig. 7 compares wave counts at $e = 2$ mm for $Ra = 1$, 1000 and 10,000, representing the diffusion-dominated, transition and vigorous-convection ranges, respectively. Holding amplitude fixed keeps mean layer thickness unchanged, so these comparisons show how wavelength modifies the concentration distribution as convection develops.

At $Ra = 1$, increasing n makes the low-concentration part of the broad PDF more prominent, slightly lowers the mean and increases I. This agrees with the low-Ra amplitude comparisons: geometry changes the concentration distribution even when overall transfer is predominantly diffusive. At $Ra = 1000$, the peak near $c = 1$ increases with n: the area fraction within $0.975 \leq c \leq 1$ rises from 0.166 at $n = 5$ to 0.344 at $n = 15$. The mean also increases, but I is smallest at $n = 10$ before rising again. The mean shift toward high concentrations and the minimum variance therefore correspond to different wave counts. At $Ra = 10{,}000$, the $n = 15$ case has a larger high-concentration contribution, a higher mean and lower I than $n = 5$, while Sh is slightly lower. This is the same qualitative combination highlighted by the $n = 10$ amplitude comparison in Table 7: weaker transfer coexists with lower variance and a shift toward the high-concentration boundary state. Spatial variance can therefore decrease while the high-concentration contribution grows, even as boundary transfer weakens.

3.5. Mean composition and the interpretation of lower variance

Mean concentration helps distinguish how a low-variance state is reached. We summarize its displacement from the midpoint of the imposed concentration range by $B = (2\langle c\rangle - 1)^2$, and evaluate $M = 4\langle c(1 - c)\rangle$, giving $I + B + M = 1$. For example, uniform fields at $c = 0.5$ and $c = 0.9$ both have $I = 0$, but B is 0 and 0.64, respectively. B is a response measure, not an additional control parameter; n, e and Ra remain the varied parameters. Because B is squared, the mean concentration or PDF is needed to identify whether the displacement is toward higher or lower concentrations. Fig. 8 shows the variation of time-averaged B and M with Ra for different wave numbers n and amplitudes e.

(1) Diffusion-dominated range ($Ra < 4\pi^2$): geometry changes both the mean and the heterogeneity. At $Ra = 1$ and 10, B is small and M is relatively large. Increasing n or e increases B and decreases M; because the corresponding mean is below 0.5, the shift is toward lower concentrations. Together with the increase in I, this shows that geometric changes to the diffusive profile make concentration more heterogeneous while shifting its mean toward the low-concentration end.

(2) Transition range ($4\pi^2 \leq Ra \leq 1300$): the development of convection is accompanied by changes in both the mean shift and the variance. As the PDF shifts toward $c = 1$, B generally exceeds its low-Ra level, while B and M exhibit geometry-dependent peaks and turning points. For $n = 5$ and $e = 6$ mm, B reaches its sampled maximum in this range at $Ra = 500$, where M is smallest; both reverse direction by $Ra = 1000$. This corresponds to the changing

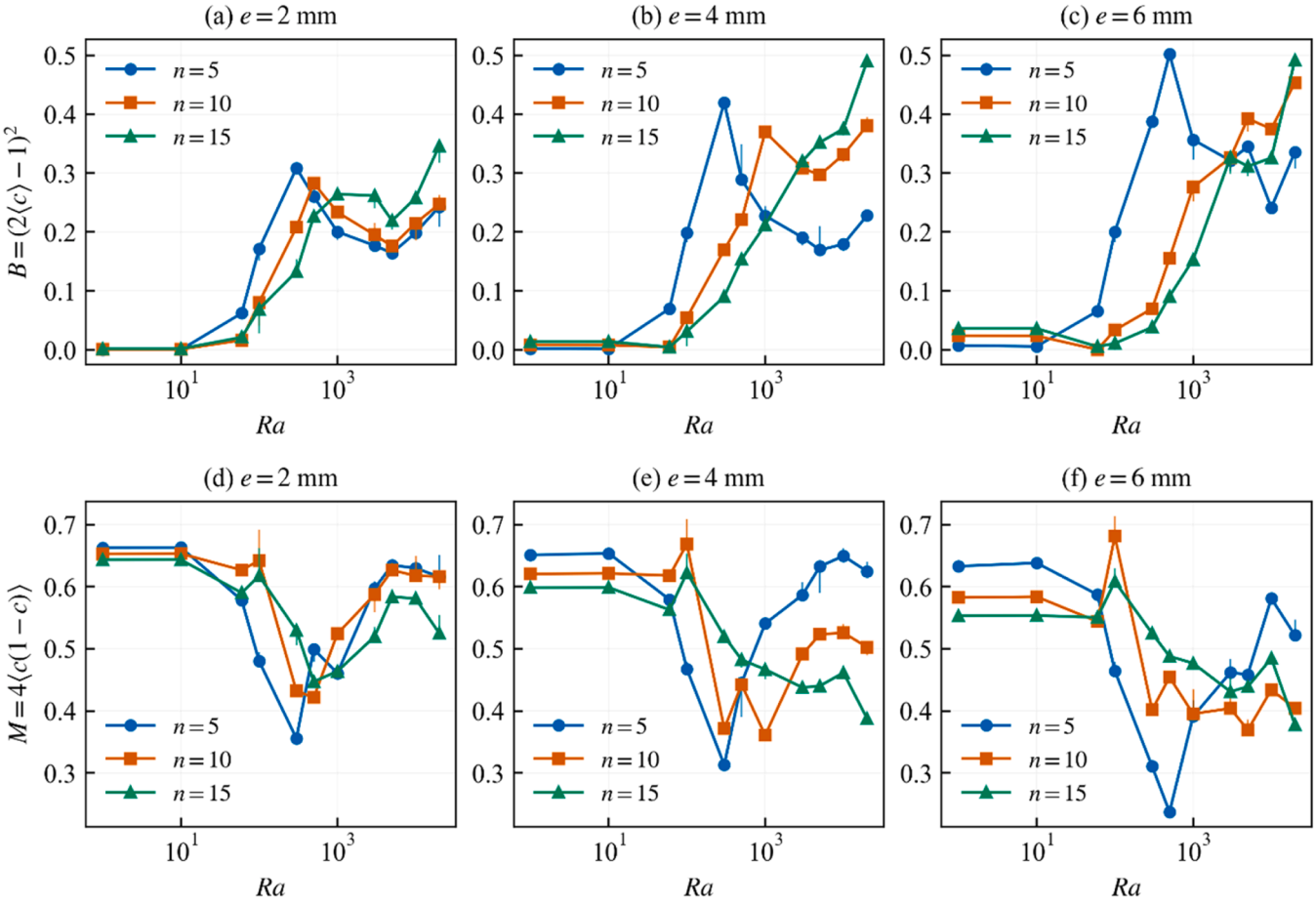

Fig. 8. Time averages of instantaneous mean-composition bias B in panels (a–c) and complementary second moment M in panels (d–f). Columns show $e = 2$, 4 and 6 mm. Each row uses a common vertical scale; geometry symbols and window-sensitivity spans follow Fig. 4. B measures displacement from the midpoint; the mean and PDF identify its direction. The identity $I + B + M = 1$ holds before averaging.

PDF peak and shows that geometry affects both the dominant concentration state and spatial heterogeneity as transfer increases.

(3) Vigorous-convection range ($Ra > 1300$): increasing uniformity can coexist with a shift toward higher concentrations. I decreases overall, but the changes in B and M remain geometry-dependent. For $n = 10$ and $e = 4$ mm, increasing Ra from 10,000 to 20,000 lowers I while raising B and lowering M. The concentration field is more uniform, but its mean shifts further toward the high-concentration state. Together with Table 7, this distinction between uniformity and mean state helps interpret transfer suppression under vigorous convection.

3.6. Representative velocity and concentration fields

Figs. 9 and 10 show representative velocity and concentration fields for $n = 5$ and $e = 2$ mm at the last saved time for each indicated Ra. Velocity magnitude is normalized by $u_b = \varphi$ D Ra / h', and the selected velocity maps use the same scale.

The two figures connect the preceding global statistics with the spatial structure of flow and concentration. At $Ra = 100$, the circulation cells in Fig. 9 are relatively regular, and the concentration field in Fig. 10 also exhibits an organized structure associated with the wavy boundary. At $Ra = 1000$, streamline directions and spatial scales become more varied, while irregular plumes and patches appear in the concentration field. This change from a relatively regular structure to spatial redistribution provides context for the non-monotonic responses of I and the PDFs in the transition range.

At $Ra = 5000$ and 20,000, the spatial structures in both figures are finer, with local plumes superimposed on broader concentration patterns. The overall reduction in I for this geometry in Fig. 5 indicates smaller concentration differences, while the PDFs in Fig. 6 show that the high-concentration part retains some weight. These fields show overall concentration homogenization together with the persistence of intermediate- and high-concentration regions.

Fig. 9 identifies flow paths and their relation to the troughs, while Fig. 10 shows the corresponding concentration differences. Together they add flow paths and local concentration contrasts to the global Sh, I and PDF statistics, providing a flow-field context for the subsequent discussion of trough-to-bulk exchange. These are instantaneous spatial patterns; transfer enhancement or suppression is assessed from the preceding time-averaged statistics and geometric comparisons.

3.7. Hydrodynamic shielding and the interpretation of transfer suppression

The results link the transfer enhancement accompanying developing convection with the geometric constraints on transfer gains in the vigorous-convection range. Hydrodynamic shielding offers a physical explanation for suppressed transfer in selected wavy geometries: fluid can circulate within a trough while exchange of low-concentration near-wall fluid with the overlying region remains restricted. The bulk concentration then becomes more strongly weighted toward the upper-boundary state. The comparisons in Table 7 and the PDFs support this interpretation, and Figs. 9 and 10 provide the corresponding spatial context. Together, the flux, concentration and field comparisons connect

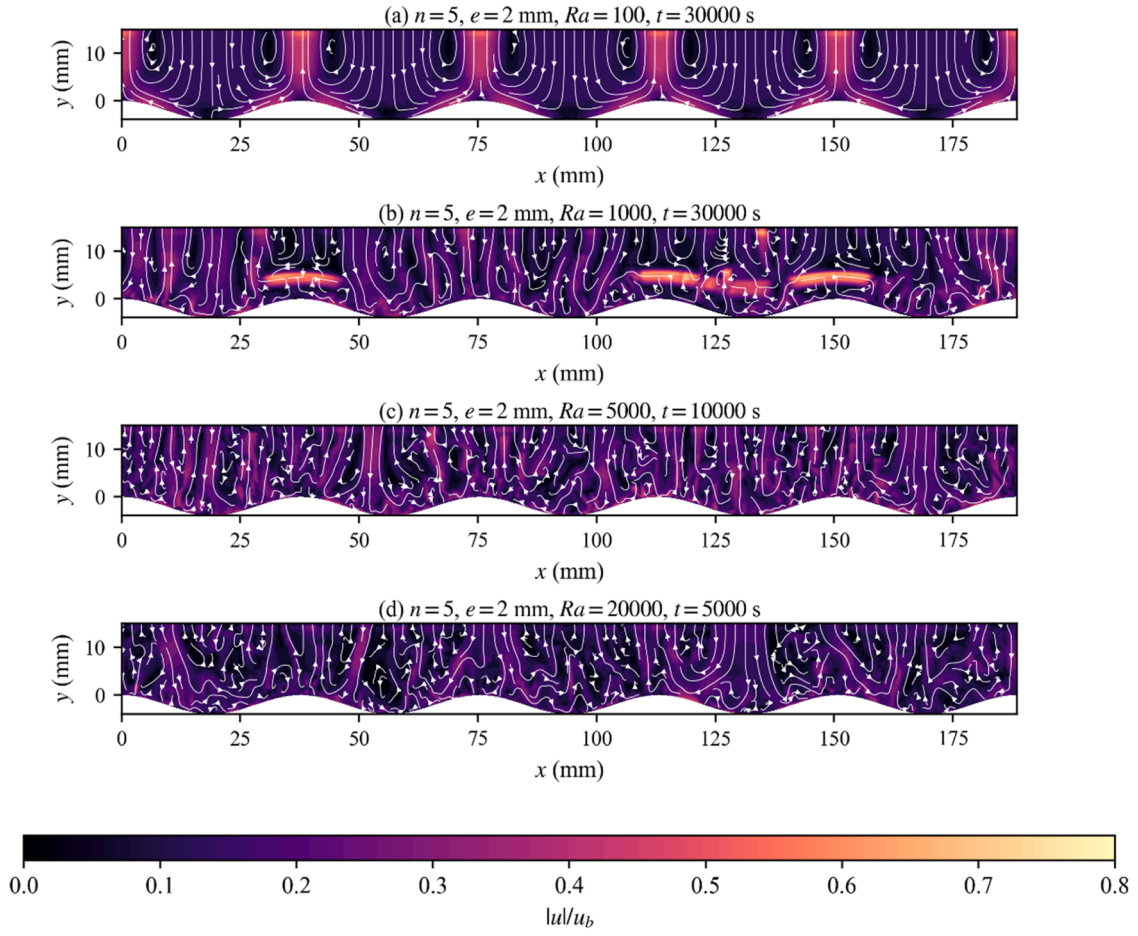

Fig. 9. Instantaneous velocity magnitude normalized by u_b for $n = 5$, $e = 2$ mm. White curves are streamlines interpolated only within the saved mesh. $Ra = 100$, $t = 30{,}000$ s; $Ra = 1000$, $t = 30{,}000$ s; $Ra = 5000$, $t = 10{,}000$ s; $Ra = 20{,}000$, $t = 5000$ s. A common velocity scale is used across the panels.

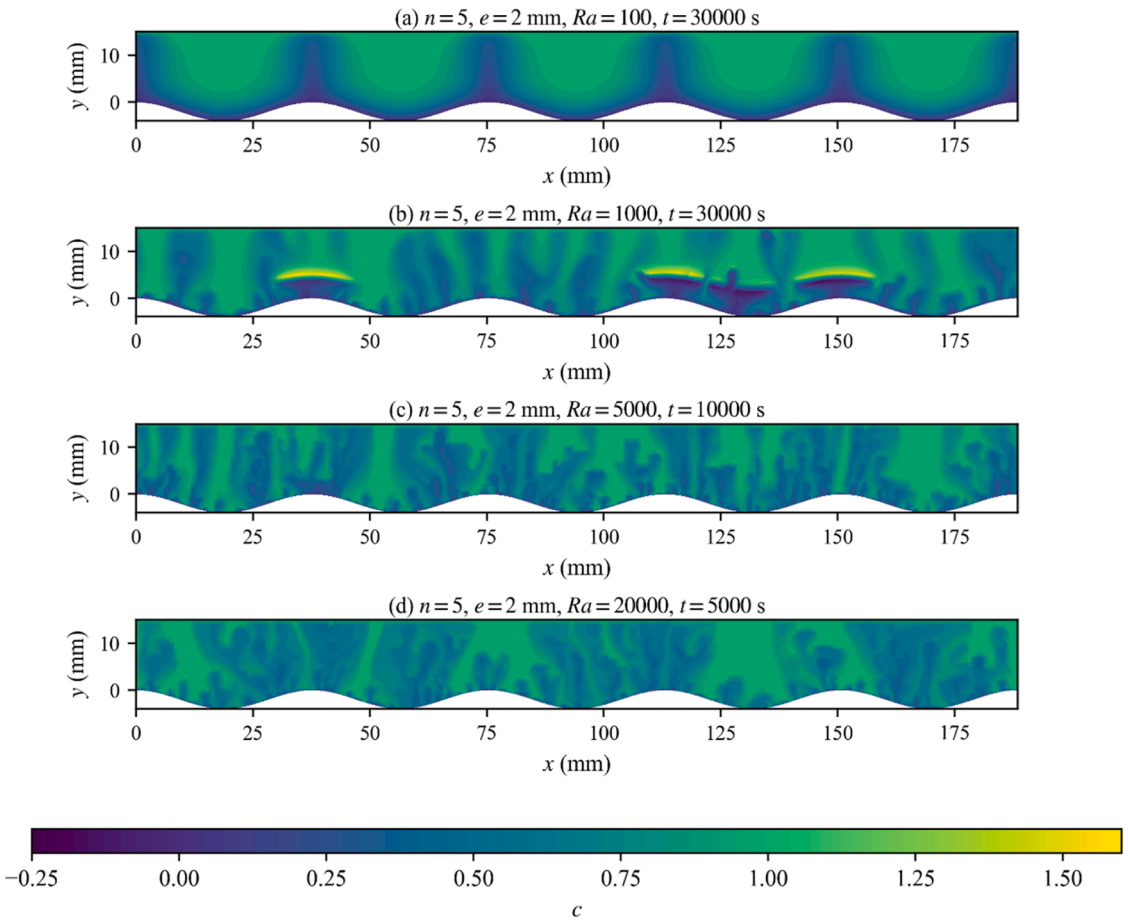

Fig. 10. Instantaneous normalized concentration for the same geometry and saved times as Fig. 9.

the shielding interpretation to the computed transport response of the fixed-interface model.

(1) Diffusion-dominated range ($Ra < 4\pi^2$): geometry changes the diffusive profile, and the wavy layers show a modest transfer enhancement relative to the flat reference. The broad PDFs and increasing I with n and e indicate that geometry also makes concentration more heterogeneous. Increasing wave count and increasing amplitude have different effects on Sh in this range and must be considered separately.
(2) Transition range ($4\pi^2 \leq Ra \leq 1300$): developing convection raises transfer above its low-Ra background, while geometry determines the gain and the redistribution of concentration. Crossings in Sh and peaks in I, B and the PDFs show how convective development couples geometric transfer gains with shifts in mean concentration and spatial redistribution. This range exhibits a growing interaction between boundary wavelength and convective structure.
(3) Vigorous-convection range ($Ra > 1300$): reduced relative transfer gains and concentration redistribution jointly support the shielding interpretation. As Ra increases, Sh grows while Sh/Ra generally declines. At a fixed Ra, selected geometric comparisons show lower Sh together with a higher mean concentration and lower I. The PDFs and B–M analysis attribute the more uniform field partly to a greater contribution from the high-concentration state. These results are consistent with restricted exchange between troughs and the overlying fluid, through which hydrodynamic shielding can weaken the influence of the low-concentration wall on the bulk.

4. Conclusion

This study used two-dimensional Darcy–Brinkman simulations to examine mass transfer and concentration redistribution above a fixed wavy boundary, with hydrodynamic shielding as a physical interpretation of geometry-dependent transfer suppression. Joint comparisons of boundary flux, segregation intensity, mean concentration and concentration PDFs lead to four conclusions.

(1) Boundary geometry regulates the transfer gain as convection develops. Transfer in the wavy layers is slightly above the flat reference in the diffusion-dominated range, and geometric differences become more pronounced as convection strengthens. Under vigorous convection, Sh increases with Ra while Sh/Ra generally declines. Increasing amplitude can enhance or suppress transfer, with a non-monotonic response in the representative sequence. Wave count and amplitude therefore act together to control the enhancement or suppression of boundary exchange.
(2) Concentration uniformity evolves with the convection regime and boundary geometry. Segregation intensity I rises with wave count and amplitude in the diffusion-dominated range, exhibits geometry-dependent peaks in the transition range, and generally decreases under vigorous convection. In selected amplitude comparisons, lower I accompanies lower Sh and a higher mean concentration. This combination identifies a more uniform concentration field that is also more strongly weighted toward the high-concentration boundary state.
(3) Concentration PDFs and the B–M decomposition separate the contributions of mean composition and spatial heterogeneity to this response. B quantifies the magnitude of the mean

displacement from the midpoint concentration, I measures spatial variance, and M is the complementary second moment. The mean concentration or PDF identifies the direction of the displacement. Together, these measures describe how the concentration state changes alongside boundary transfer.

(4) Hydrodynamic shielding links transfer suppression with concentration redistribution under vigorous convection. Restricted exchange between troughs and the overlying fluid can weaken the influence of the low-concentration wall on the bulk, accounting for weaker transfer together with a shift toward the high-concentration state. Joint flux and concentration statistics support this interpretation, with velocity and concentration fields providing its spatial context.

Developing convection enhances boundary transfer, while at higher Ra the wavy layers show an overall decline in Sh/Ra and geometry-dependent transfer suppression. The associated concentration redistribution supports hydrodynamic shielding through restricted trough-to-bulk exchange as an explanation of this response. This relationship among interface geometry, transfer and concentration state provides a physical basis for interpreting solute exchange across non-planar interfaces in saline groundwater and geological carbon-storage systems.

Funding

We gratefully acknowledge the financial support provided by the Young Scientists Fund (C) of the National Natural Science Foundation of China (Grant No. 12602407), the China Postdoctoral Science Foundation (Grant No. 2025M781758), the National Key Research and Development Program of China (Grant No. 2023YFC3011300), and the National Key Research and Development Program of China (Grant No. 2021YFA0717200).

Declaration of generative AI and AI-assisted technologies in the manuscript preparation process

OpenAI ChatGPT/Codex was used to assist with revision and consistency checks, and with preparation of post-processing and plotting scripts. Numerical results originate from COMSOL solutions.

CRediT authorship contribution statement

Yumin Wang: Writing – review & editing, Writing – original draft, Visualization, Validation, Software, Methodology, Investigation, Formal analysis, Data curation, Conceptualization. **Jiansong Wu:** Writing – review & editing, Supervision, Resources, Project administration, Funding acquisition. **Ke Xu:** Writing – review & editing, Supervision, Resources, Methodology, Funding acquisition, Data curation, Conceptualization.

Declaration of competing interest

for "*Hydrodynamic Shielding and Non-monotonic Mass Transfer in Porous Media Convection*"

We declare no conflict of interest.

Data availability

Data will be made available on request.

References

Amooie, M.A., Soltanian, M.R., Moortgat, J., 2018. Solutal convection in porous media: comparison between boundary conditions of constant concentration and constant flux. Phys. Rev. E 98, 033118. https://doi.org/10.1103/PhysRevE.98.033118.

Backhaus, S., Turitsyn, K., Ecke, R.E., 2011. Convective instability and mass transport of diffusion layers in a hele-shaw geometry. Phys. Rev. Lett. 106, 104501. https://doi.org/10.1103/PhysRevLett.106.104501.

Biswas, N., Chatterjee, D., Sarkar, S., Manna, N.K., 2024. Magneto-nanofluidic thermal transport and irreversibility in semicircular systems with heated wavy bottom under constant fluid volume and cooling surface constraints. Int. J. Numer. Methods Heat. Fluid. Flow. 34, 1021–1059. https://doi.org/10.1108/HFF-06-2023-0354.

De Paoli, M., 2023. Convective mixing in porous media: a review of darcy, pore-scale and hele-shaw studies. Eur. Phys. J. E 46, 129. https://doi.org/10.1140/epje/s10189-023-00390-8.

De Paoli, M., Howland, C.J., Verzicco, R., Lohse, D., 2024. Towards the understanding of convective dissolution in confined porous media: thin bead pack experiments, two-dimensional direct numerical simulations and physical models. J. Fluid. Mech. 987, A1. https://doi.org/10.1017/jfm.2024.328.

De Paoli, M., Zonta, F., Soldati, A., 2016. Influence of anisotropic permeability on convection in porous media: implications for geological CO2 sequestration. Phys. Fluids 28, 056601. https://doi.org/10.1063/1.4947425.

Hewitt, D.R., 2020. Vigorous convection in porous media. Proc. R. Soc. A: Math. Phys. Eng. Sci. 476, 20200111. https://doi.org/10.1098/rspa.2020.0111.

Hewitt, D.R., Neufeld, J.A., Lister, J.R., 2012. Ultimate regime of high rayleigh number convection in a porous medium. Phys. Rev. Lett. 108, 224503. https://doi.org/10.1103/PhysRevLett.108.224503.

Hidalgo, J.J., Fe, J., Cueto-Felgueroso, L., Juanes, R., 2012. Scaling of convective mixing in porous media. Phys. Rev. Lett. 109, 264503. https://doi.org/10.1103/PhysRevLett.109.264503.

Hussain, S., 2025. Hydrodynamic and thermosolutal analysis of MHD ternary hybrid nanofluids in BFS configuration: high-order FEM for drag reduction and thermal enhancement. Int. J. Numer. Methods Heat. Fluid. Flow. 35, 2577–2607. https://doi.org/10.1108/HFF-04-2025-0291.

Hussain, S., Chattopadhyay, A., Almutairi, B., Hansda, S., 2026. Non-newtonian casson fluid double diffusion magneto-hydrodynamics in a concentric ring with different cylinders containing radiative ternary nanofluids. Int. J. Numer. Methods Heat. Fluid. Flow. 36, 1406–1437. https://doi.org/10.1108/HFF-10-2025-0792.

Hussain, S., Prakash, J., Almutairi, B., Ramesh, K., 2025. Numerical simulation of double-diffusive convection in hybrid nanofluid flow in a porous medium within a swastika-shaped cavity. Int. J. Numer. Methods Heat. Fluid. Flow. 35, 2356–2381. https://doi.org/10.1108/HFF-01-2025-0062.

Li, J., Yang, Y., Sun, C., 2025. From Darcy convection to free-fluid convection: pore-scale study of density-driven currents in porous media. J. Fluid. Mech. 1009, A10. https://doi.org/10.1017/jfm.2025.213.

Mandal, D.K., Manna, N.K., Biswas, N., Rudra, T., Kumar, R., Benim, A.C., 2026. Enhanced heat transport in magneto-nanofluidic thermal systems: adiabatic block effects in grooved channels and ANN modeling. Int. J. Thermofluids 31, 101515. https://doi.org/10.1016/j.ijft.2025.101515.

Manna, N.K., Biswas, N., Mandal, D.K., Yadav, C.K., 2025. Steady and unsteady dynamics of magneto-nanofluidic flow in a bottom-heated top-cooled recto-triangular thermal system. Heat. Transfer. Eng. 46, 400–420. https://doi.org/10.1080/01457632.2024.2317611.

Post, V.E.A., Groen, J., Kooi, H., Person, M., Ge, S., Edmunds, W.M., 2013. Offshore fresh groundwater reserves as a global phenomenon. Nature 504, 71–78. https://doi.org/10.1038/nature12858.

Rahaman, M.M., Biswas, N., Santra, A.K., Manna, N.K., 2024. Effects of heater positions on magneto-hydrodynamic convection of CuO-water nanofluid flow in a grooved channel. Int. J. Numer. Methods Heat. Fluid. Flow. 34, 1699–1729. https://doi.org/10.1108/HFF-11-2023-0695.

Rees, D.A.S., 2002. The onset of Darcy–Brinkman convection in a porous layer: an asymptotic analysis. Int. J. Heat. Mass Transf. 45, 2213–2220. https://doi.org/10.1016/S0017-9310(01)00332-5.

Ruan, L., Rybak, I., 2025. A hybrid-dimensional stokes–brinkman–darcy model for arbitrary flows to the fluid–porous interface. Transp. Porous. Media 152, 75. https://doi.org/10.1007/s11242-025-02220-1.

Ruan, L., Rybak, I., 2026. Stokes–Brinkman–Darcy models for fluid–porous systems: derivation, analysis and validation. Appl. Math. Comput. 510, 129687. https://doi.org/10.1016/j.amc.2025.129687.

Schwendener, D., Noir, J., Latt, J., Coreixas, C., Kong, X.-Z., 2026. Natural convection in porous media: the role of porosity and conductivity ratios in the transition from laminar to inertial convection. J. Fluid. Mech. 1026, A21. https://doi.org/10.1017/jfm.2025.11014.

Wang, Y., Wu, J., Xu, K., 2026. Non-straight boundary regulates natural convection pattern in porous media. Int. J. Heat. Mass Transf. 268, 129024. https://doi.org/10.1016/j.ijheatmasstransfer.2026.129024.

Wang, Y., Xie, J.-H., Yang, W., Li, X., Abulaiti, Z., Zheng, S., Zhu, J., Xu, K., 2025. Permafrost thawing under overlaying salt water. Sci. Adv. 11, eadp2808. https://doi.org/10.1126/sciadv.adp2808.

Zhu, X., Fu, Y., De Paoli, M., 2024. Transport scaling in porous media convection. J. Fluid. Mech. 991, A4. https://doi.org/10.1017/jfm.2024.528.